Calibration and sensitivity of the Virgo detector during its second science run

2011 Class. Quantum Grav. 28 025005

(http://iopscience.iop.org/0264-9381/28/2/025005)

IOP Publishing Classical and Quantum Gravity

Class. Quantum Grav. 28 (2011) 025005 (25pp) doi:10.1088/0264-9381/28/2/025005

Calibration and sensitivity of the Virgo detector during its second science run

T Accadia[1], F Acernese[2ac], F Antonucci[3a], P Astone[3a], G Ballardin[4], F Barone[2ac], M Barsuglia[5], A Basti[6ab], Th S Bauer[7a], M G Beker[7a], A Belletoile[1], S Birindelli[8a], M Bitossi[6a], M A Bizouard[9a], M Blom[7a], F Bondu[8b], L Bonelli[6ab], R Bonnand[10], V Boschi[6a], L Bosi[11a], B Bouhou[5], S Braccini[6a], C Bradaschia[6a], A Brillet[8a], V Brisson[9a], R Budzyński[12b], T Bulik[12cd], H J Bulten[7ab], D Buskulic[1], C Buy[5], G Cagnoli[13a], E Calloni[2ab], E Campagna[13ab], B Canuel[4], F Carbognani[4], F Cavalier[9a], R Cavalieri[4], G Cella[6a], E Cesarini[13b], O Chaibi[8a], E Chassande Mottin[5], A Chincarini[14], F Cleva[8a], E Coccia[15ab], C N Colacino[6ab], J Colas[4], A Colla[3ab], M Colombini[3b], A Corsi[3a], J-P Coulon[8a], E Cuoco[4], S D'Antonio[15a], V Dattilo[4], M Davier[9a], R Day[4], R De Rosa[2ab], G Debreczeni[16], M del Prete[6ac], L Di Fiore[2a], A Di Lieto[6ab], M Di Paolo Emilio[15ac], A Di Virgilio[6a], A Dietz[1], M Drago[17cd], V Fafone[15ab], I Ferrante[6ab], F Fidecaro[6ab], I Fiori[4], R Flaminio[10], L A Forte[2a], J-D Fournier[8a], J Franc[10], S Frasca[3ab], F Frasconi[6a], A Freise[18], M Galimberti[10], L Gammaitoni[11ab], F Garufi[2ab], M E Gáspár[16], G Gemme[14], E Genin[4], A Gennai[6a], A Giazotto[6a], R Gouaty[1], M Granata[5], C Greverie[8a], G M Guidi[13ab], J-F Hayau[8b], H Heitmann[8], P Hello[9a], S Hild[19], D Huet[4], P Jaranowski[12e], I Kowalska[12c], A Królak[12af], N Leroy[9a], N Letendre[1], T G F Li[7a], N Liguori[17ab], M Lorenzini[13a], V Loriette[9b], G Losurdo[13a], E Majorana[3a], I Maksimovic[9b], N Man[8a], M Mantovani[6ac], F Marchesoni[11a], F Marion[1], J Marque[4], F Martelli[13ab], A Masserot[1], C Michel[10], L Milano[2ab], Y Minenkov[15a], M Mohan[4], N Morgado[10], A Morgia[15ab], S Mosca[2ab], V Moscatelli[3a], B Mours[1], I Neri[11ab], F Nocera[4], G Pagliaroli[15ac], L Palladino[15ac], C Palomba[3a], F Paoletti[4,6a], S Pardi[2ab], M Parisi[2b], A Pasqualetti[4], R Passaquieti[6ab], D Passuello[6a], G Persichetti[2ab], M Pichot[8a], F Piergiovanni[13ab], M Pietka[12e], L Pinard[10], R Poggiani[6ab], M Prato[14], G A Prodi[17ab], M Punturo[11a], P Puppo[3a], D S Rabeling[7ab], I Rácz[16], P Rapagnani[3ab], V Re[17ab], T Regimbau[8a], F Ricci[3ab], F Robinet[9a], A Rocchi[15a], L Rolland[1], R Romano[2ac], D Rosińska[12g], P Ruggi[4], B Sassolas[10], D Sentenac[4], L Sperandio[15ab], R Sturani[13ab], B Swinkels[4], M Tacca[4], A Toncelli[6ab], M Tonelli[6ab], O Torre[6ac], E Tournefier[1], F Travasso[11ab], G Vajente[6ab], J F J van den Brand[7ab], S van der Putten[7a], M Vasuth[16], M Vavoulidis[9a], G Vedovato[17c], D Verkindt[1], F Vetrano[13ab], A Viceré[13ab], J-Y Vinet[8a], H Vocca[11a], R L Ward[5], M Was[9a] and M Yvert[1]

[1] Laboratoire d'Annecy-le-Vieux de Physique des Particules (LAPP), Université de Savoie, CNRS/IN2P3, F-74941 Annecy-Le Vieux, France

0264-9381/11/025005+25$33.00 © 2011 IOP Publishing Ltd Printed in the UK & the USA

[2] INFN, Sezione di Napoli[a]; Università di Napoli 'Federico II[b]' Complesso Universitario di Monte S. Angelo, I-80126 Napoli; Università di Salerno, Fisciano, I-84084 Salerno[c], Italy
[3] INFN, Sezione di Roma[a]; Università 'La Sapienza'[b], I-00185 Roma, Italy
[4] European Gravitational Observatory (EGO), I-56021 Cascina (PI), Italy
[5] Laboratoire AstroParticule et Cosmologie (APC) Université Paris Diderot, CNRS: IN2P3, CEA: DSM/IRFU, Observatoire de Paris 10, rue A. Domon et L. Duquet, 75013 Paris, France
[6] INFN, Sezione di Pisa[a]; Università di Pisa[b]; I-56127 Pisa; Università di Siena, I-53100 Siena[c], Italy
[7] Nikhef, National Institute for Subatomic Physics, PO Box 41882, 1009 DB Amsterdam[a]; VU University Amsterdam, De Boelelaan 1081, 1081 HV Amsterdam[b], The Netherlands
[8] Université Nice-Sophia-Antipolis, CNRS, Observatoire de la Côte d'Azur, F-06304 Nice[a]; Institut de Physique de Rennes, CNRS, Université de Rennes 1, 35042 Rennes[b], France
[9] LAL, Université Paris-Sud, IN2P3/CNRS, F-91898 Orsay[a]; ESPCI, CNRS, F-75005 Paris[b], France
[10] Laboratoire des Matériaux Avancés (LMA), IN2P3/CNRS, F-69622 Villeurbanne, Lyon, France
[11] INFN, Sezione di Perugia[a]; Università di Perugia[b], I-06123 Perugia, Italy
[12] IM-PAN 00-956 Warsaw[a]; Warsaw University 00-681 Warsaw[b]; Astronomical Observatory Warsaw University 00-478 Warsaw[c]; CAMK-PAN 00-716 Warsaw[d]; Białystok University 15-424 Białystok[e]; IPJ 05-400 Świerk-Otwock[f]; Institute of Astronomy 65-265 Zielona Góra[g], Poland
[13] INFN, Sezione di Firenze, I-50019 Sesto Fiorentino[a]; Università degli Studi di Urbino 'Carlo Bo', I-61029 Urbino[b], Italy
[14] INFN, Sezione di Genova, I-16146 Genova, Italy
[15] INFN, Sezione di Roma Tor Vergata[a]; Università di Roma Tor Vergata, I-00133 Roma[b]; Università dell'Aquila, I-67100 L'Aquila[c], Italy
[16] RMKI, H-1121 Budapest, Konkoly Thege Miklós út 29-33, Hungary
[17] INFN, Gruppo Collegato di Trento[a] and Università di Trento[b], I-38050 Povo, Trento, Italy; INFN, Sezione di Padova[c] and Università di Padova[d], I-35131 Padova, Italy
[18] University of Birmingham, Birmingham B15 2TT, UK
[19] University of Glasgow, Glasgow G12 8QQ, UK

E-mail: rollandl@in2p3.fr

Received 27 September 2010, in final form 19 November 2010
Published 21 December 2010
Online at stacks.iop.org/CQG/28/025005

Abstract

The Virgo detector is a kilometer-length interferometer for gravitational wave detection located near Pisa (Italy). During its second science run (VSR2) in 2009, 6 months of data were accumulated with a sensitivity close to its design. In this paper, the methods used to determine the parameters for sensitivity estimation and gravitational wave reconstruction are described. The main quantities to be calibrated are the frequency response of the mirror actuation and the sensing of the output power. Focus is also put on their absolute timing. The monitoring of the calibration data and the parameter estimation with independent techniques are discussed to provide an estimation of the calibration uncertainties. Finally, the estimation of the Virgo sensitivity in the frequency domain is described and typical sensitivities measured during VSR2 are shown.

PACS numbers: 95.30.Sf, 04.80.Nn

(Some figures in this article are in colour only in the electronic version)

1. Introduction

The Virgo detector [1], located near Pisa (Italy), is one of the most sensitive instruments for direct detection of gravitational waves (GW) emitted by astrophysical compact sources at frequencies between 10 Hz and 10 kHz. It is an interferometer (ITF) with 3 km Fabry–Perot cavities in the arms. Typical detectable length variations are of the order of 10^{-19} m.

The Virgo second science run (VSR2) lasted from 3 July 2009 to 8 January 2010 with a sensitivity close to its nominal one, and in coincidence to the first part of the 6th science run (S6) of the LIGO detectors [2]. The data of all the detectors are used together to search for a GW signal. In the case of a detection, the combined use of all the data would increase the confidence of the detection and allow the estimation of the GW source direction and parameters.

The GW strain couples into the length degrees of freedom of the ITF. To achieve optimum sensitivity, the positions of the different mirrors are controlled [9] to have, in particular, beam resonance in the cavities, destructive interference at the ITF output port and to compensate for environmental noise. The control bandwidth would modify the ITF response to passing GW below a few hundreds hertz. Above a few hundred hertz, the mirrors behave as free falling masses; the main effect of a passing GW would then be a frequency-dependent variation of the output power of the ITF, characterized by the ITF optical response.

The main purposes of the Virgo calibration are (i) to estimate the ITF sensitivity to the GW strain as a function of frequency, $S_h(f)$ and (ii) to reconstruct the amplitude $h(t)$ of the GW strain from the ITF data. It deals with the *longitudinal*[20] differential length of the ITF arms, $\Delta L = L_x - L_y$. In the long wavelength approximation (see section 2.3 in [10]), it is related to the GW strain h by

$$h = \frac{\Delta L}{L} \qquad \text{where } L = 3\,\text{km}. \tag{1}$$

The response of the mirror actuation to the longitudinal controls have thus to be calibrated, as well as the readout electronics of the output power and the ITF optical response. Absolute timing is also a critical parameter for multi-detector analysis, in particular to determine the direction of the GW source in the sky.

The scope of this paper is restricted to the estimation of the calibration parameters and to the description of the ITF sensitivity estimation in the frequency domain. The methods and performance of the calibration procedures are given after a brief description of the Virgo detector. The way the calibration parameters are used to estimate the Virgo sensitivity is then detailed. Finally, the Virgo sensitivity measured during VSR2 is presented.

2. The Virgo detector

The optical configuration of the Virgo ITF is shown in figure 1. All the mirrors of the ITF are suspended to a chain of pendulum for seismic isolation. The input beam is produced by a Nd:YAG laser with a wavelength of $\lambda = 1064$ nm. Each arm contains a 3 km long Fabry–Perot cavity of finesse 50 whose role is to increase the optical path. The ITF arm length difference is controlled to obtain a destructive interference at the ITF output port. The power recycling (PR) mirror increases the amount of light impinging on the Michelson beam splitter (BS) by a factor of 40 [1] and as a consequence improves the ITF sensitivity. The main signal of the ITF is the light power at the output port, the so-called *dark fringe* signal.

[20] The ‘longitudinal’ direction is perpendicular to the mirror surface.

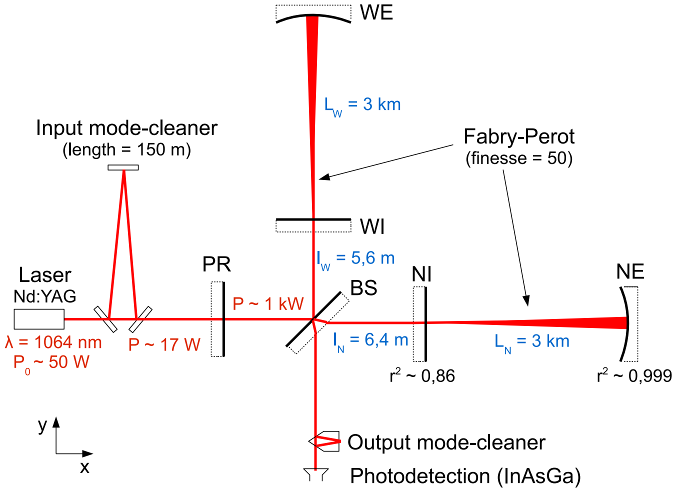

Figure 1. Optical scheme of Virgo.

Data from the ITF are time series, digitized at 10 kHz or 20 kHz, which record the optical power of various beams and different control signals.

In order to analyze in coincidence the reconstructed GW strain from different detectors, the data are time-stamped using the global positioning system (GPS).

2.1. *Mirror longitudinal actuation*

The Virgo mirrors are suspended to a complex seismic isolation system [3]. The last stage is a double-stage system with the so-called *marionette* [4] as the first pendulum. The mirror and its reaction mass are suspended to the marionette by pairs of thin steel wires.

Acting on the marionette, it is possible to translate the suspended mirror along the beam. This steering is performed by a set of coils. Each coil acts on a permanent magnet attached on the marionette.

Four additional coils supported by the recoil mass allow us to act directly on four magnets glued on the back of the mirror. It induces a mirror motion keeping a fixed center of gravity of the suspended system $\{$mirror+recoil mass$\}$.

Above 10 Hz, the longitudinal controls are distributed between the marionette up to a few 10s of Hz and the mirror up to a few 100s of Hz. Therefore, for calibration purpose, the marionette and mirror actuation responses need to be measured only up to $\sim$100 Hz and up to $\sim$1 kHz, respectively.

The actuation is used to convert a digital control signal (called zC hereafter, in V) into the mirror motion ΔL through an electromagnetic actuator and the pendulum. The actuator is composed of a digital computing part (DSP), a DAC with its anti-image filter and the analog electronics (so-called coil driver) which converts the DAC output voltage into a current flowing in the coil. The electronics can be set into two configurations: (i) a mode to acquire the lock of the ITF, the so-called high power (HP) mode; and (ii) a low noise (LN) mode with reduced dynamic to control the lock of the ITF. Different analog filters (poles and zeros) and resistors (gains) are used in the coil driver as function of the configuration. Compensating digital filters and gains are set accordingly in the DSP such that the transfer function (TF) of the actuator (in A V^{-1}) is independent of the configuration at first order[21].

The mirror motion induced by the actuators is then filtered by the pendulum mechanical response. The response to the mirror motion is modeled by a second order low-pass filter P_{mir} with a resonant frequency 0.6 Hz and a quality factor arbitrarily set to 1000 [5]. For the mirror motion induced through the marionette, the 2-stage pendulum P_{mar} has been parameterized in the calibration procedure as a series of two such filters.

The dc gain of the mirror actuation can be estimated within $\sim$10% from the nominal values of the conversion factors of the coil driver electronics γ, the current-force conversion factor α and the mechanical response of the pendulum. During VSR2, the conversion factors γ and α are respectively 1.15 A V^{-1} and 1.9 mN A^{-1} for the end mirrors and 0.10 A V^{-1} and 10.6 mN A^{-1} for the BS mirror [6]. The pendulum can be modeled by a simple pendulum with length $l = 0.7$ m and with mirror masses of $M_e = 20.3$ kg [7] and $M_{\text{BS}} = 5$ kg [8] for the end and BS mirrors respectively. The longitudinal motion of the mirrors is controlled by n_{coils} coils: two for the end mirrors and four for the BS mirror. The estimated actuation gain, perpendicular to the mirror surface, is thus

$$A = \frac{F_V}{M \times \frac{g_N}{l}} = \frac{n_{\text{coils}}\gamma\alpha}{M \times \frac{g_N}{l}} \tag{2}$$

where F_V is the force per unit volt and $g_N = 9.81\,\text{m s}^{-2}$ is the standard gravitational acceleration. With the numbers given above, the gains for the end and BS mirrors are expected to be 15.1 μm V^{-1} and 61 μm V^{-1} respectively. For a motion ΔL_{BS} of the BS mirror, the length of the west arm is left unchanged while the length of the north arm varies by $\sqrt{2}\,\Delta L_{\text{BS}}$. The effective gain on the differential arm length variation is thus expected to be $61\sqrt{2} \sim 86\,\mu$m V^{-1}.

2.2. *Sensing of the ITF output power*

In order to control the ITF [9], the laser beam is phase modulated. The main signal of the ITF is the demodulated output power called $\mathcal{P}_{\text{ac}}$.

The output power of the ITF is sensed using two photodiodes. Their signals then go through preamplifiers, demodulation boards and ADCs with anti-alias filters. Both raw demodulated signals, digitized at 20 kHz, are then sent into a digital process where they are summed to compute the output port channel $\mathcal{P}_{\text{ac}}$. In the following, the TF from the power at the output port to the measured signal will be called S.

In the sensing process, the total power of the output beam is also read out and stored in the channel $\mathcal{P}_{\text{dc}}$.

2.3. *Longitudinal control loop*

The longitudinal control loop [9] used to lock the ITF on a *dark fringe* in the *science mode* (standard data taking conditions) is summarized in figure 2. The error signal is the ITF output power $\mathcal{P}_{\text{ac}}$ (W), readout through photodiodes and their associated electronics with response S. Filters F_i (V W^{-1}) are used to define the control signals sent to the different actuation channels (controlled mirrors: NE, WE, BS, PR, and marionettes: NE, WE, indicated by the subscript i). The signal is then sent to the actuator with response $A_i \times P_i$ (m V^{-1}) in order to move the mirror (P_i is the mechanical response of the pendulum and A_i the part of the response due

---

[21] Mis-compensations are measured, see section 4.2.

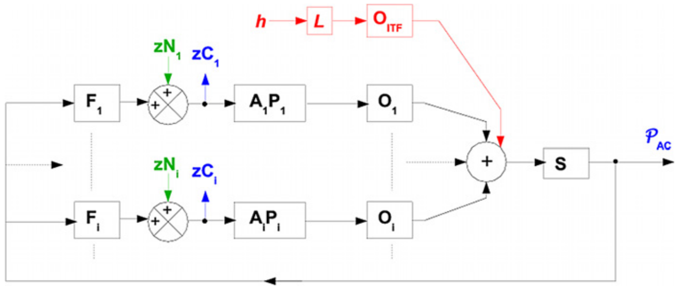

Figure 2. Overview diagram of the longitudinal control loop. For the actuation channel i: A_i and P_i are the actuator and pendulum responses, O_i is the ITF optical response. S is the TF of the sensing of the ITF output power $\mathcal{P}_{\rm ac}$, used as the error signal. F_i is the TF of the global control loop. The actuation entries are the control signal and the calibration signal zN_i. The sum of both gives the signal zC_i. The GW signal $h(t)$ enters the ITF as a differential motion of the two cavity end mirrors.

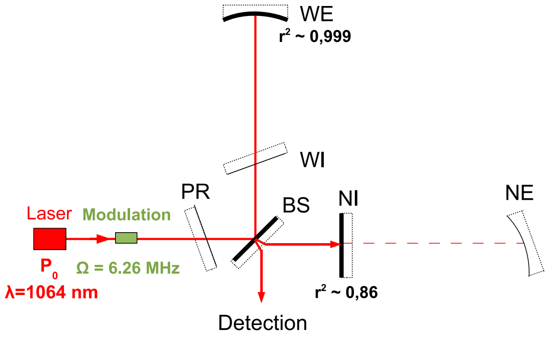

Figure 3. Example of asymmetric (NI–WE) Michelson configuration. The mirror reflective surfaces are shown with continuous lines. The surfaces that constitute the Michelson ITF are the bold lines. The tilted mirrors do not participate in the output signal (except for an attenuation of the laser power).

to the electromagnetic actuator). The ITF output power depends on the mirror positions and determines the optical response O_i of the interferometer (W m^{-1}).

A calibration signal zN_i can be added at the input of the actuation. The sum of the control signal and of the calibration signal is readout as zC_i.

3. Absolute length measurement

The ITF calibration requires absolute length measurements. The displacement induced by the mirror actuators is reconstructed from the ITF setup as the simple Michelson (see for example figure 3) using the laser wavelength as the length reference and its nonlinear response when the fringes are passing.

The method is first described. Corrections due to the ITF optical response and the power readout response are then highlighted.

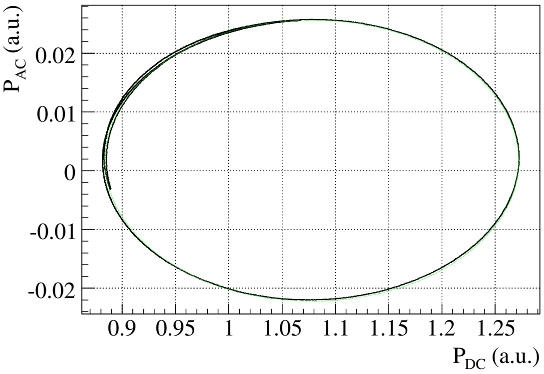

Figure 4. Example of the ac versus dc signals in a free swinging Michelson configuration (asymmetric Michelson) along with the fitted ellipse (green curve).

3.1. Output powers

In a simple Michelson ITF, the phase difference $\Delta\Phi$ between the two interfering beams is a function of the differential arm length ΔL, and the laser wavelength $\lambda = 1064$ nm:

$$\Delta\Phi(t) = \frac{4\pi}{\lambda}\Delta L(t). \tag{3}$$

In a simple Michelson ITF with frontal phase modulation, the continuous ($\mathcal{P}_{\text{dc}}$) and demodulated ($\mathcal{P}_{\text{ac}}$) signals of the output beam are the functions of the phase difference $\Delta\Phi$ between the two interfering beams [11]:

$$\mathcal{P}_{\text{dc}} = \beta(1 - \gamma\cos(\Delta\Phi)) \tag{4}$$

$$\mathcal{P}_{\text{ac}} = \alpha\sin(\Delta\Phi) \tag{5}$$

where α and β are proportional to the laser power and γ is proportional to the ITF contrast. Therefore, in the ($\mathcal{P}_{\text{dc}}, \mathcal{P}_{\text{ac}}$) plane, the signals follow an ellipse as shown in figure 4.

3.2. Nonlinear reconstruction method

The measurement of the differential arm length ΔL uses a nonlinear reconstruction. The ellipse followed by the $\mathcal{P}_{\text{ac}}$ and $\mathcal{P}_{\text{dc}}$ signals is fitted [12]. The fit gives the ellipse center position and the axis widths. In order to follow their possible time variations, the parameters are estimated every time the phase has changed by 2π, which correspond to a few times per second. During the few minutes long datasets used for calibration, the typical variations are of the order of 1% on the ellipse widths and center. The angle between the ellipse axis along dc and the line from the ellipse center to the present point position ($\mathcal{P}_{\text{dc}}, \mathcal{P}_{\text{ac}}$) can then be estimated directly for every sample of the ITF signals. Using a suitable ellipse tour counting, the right number of 2π is added to recover completely the angle $\Delta\Phi$. The differential arm length ΔL_{rec} is then computed using equation (3).

An illustration of the method is shown in figure 5.

The typical sensitivity of the free swinging Michelson is given by the spectrum of the reconstructed ΔL_{rec} channel as shown in figure 6. The sensitivity is of the order of 10^{-9} m or below at few Hz and down to 3×10^{-13} m above 1 kHz. The limiting noise sources have been determined from SIESTA simulation [13]. It comes from seismic noise below 1 Hz, a mix of

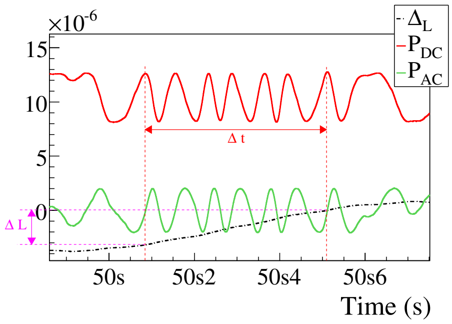

Figure 5. Reconstructed ΔL signal along with the dc and ac powers as a function of time in asymmetric WE–NI Michelson configuration data. The unit of the y-axis depends on the signal: 1 m for ΔL, 10 W for the ac power and 20 W for the dc power. In the window Δt, six interfringes passed on the dc signal. It indicates a differential arm elongation of $\Delta L = 6 \times \frac{\lambda}{2} = 3.19\,\mu\text{m}$.

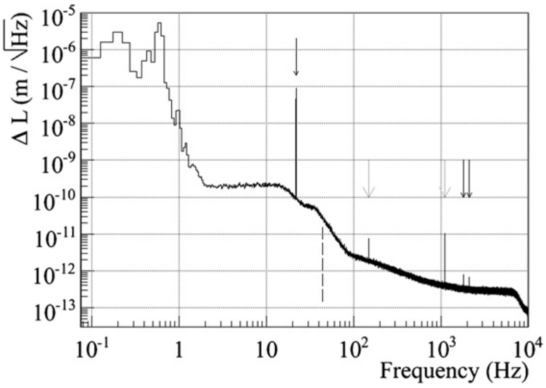

Figure 6. Typical noise level (FFT) of the reconstructed ΔL signal in free swinging Michelson data (asymmetric configuration). The resonance frequency of the pendulum is visible around 0.6 Hz. One power line is visible at 150 Hz. The line used for the laser frequency stabilization control loop is seen at 1111 Hz. The mirrors were excited at three frequencies shown by the dark arrows (22.0 Hz, 1816.5 Hz and 2116.5 Hz). In presence of nonlinearities, the first harmonic of the strong 22 Hz line would have been visible at 44 Hz (dashed line). Note that the symmetric Michelson configuration using the two end mirrors, NE and WE, is not used since the noise level is higher.

seismic noise and laser power noise up to ∼20 Hz, power noise up to ∼1 kHz and ADC noise at higher frequency.

The reconstruction method has been applied to simulated data produced by the SIESTA code. No systematic error due to the method was found between 1 Hz and 10 kHz within 0.01% when comparing the reconstructed ΔL with the simulated one.

Since the laser wavelength is precisely known, bias in the method could only arise between fringes. When inducing sine motion to the mirrors, this would show up as harmonic lines in the spectrum of the reconstructed ΔL_{rec}. Such lines were not found above the noise level (see figure 6). It indicates that possible nonlinearities on the main line amplitude, and therefore on the absolute length calibration, are lower than 0.1%.

3.3. Measured signals

The differential mirror motion of the Michelson is converted by the ITF optical response O_{Mich} into a power at the output port. The power is sensed with response S to get the output channels $\mathcal{P}_{\mathrm{dc}}$ and $\mathcal{P}_{\mathrm{ac}}$. Both responses have to be taken into account to reconstruct properly the differential length ΔL:

- In free swinging Michelson configurations, O_{Mich} is simply a delay due to the light propagation time from the moving mirror to the photodiode: $10\,\mu$s for the end mirrors (3 km) and 0 for the input mirrors (the propagation time in the central part can be neglected). For the BS mirror, a delay of $10\,\mu$s is expected when the WE mirror is used, and no delay when the WI mirror is used.
- Below 2 kHz, S is equivalent to a delay of $49.3\,\mu$s from the GPS time (see section 5).

4. Actuation calibration

The actuation response calibration consists in measuring the longitudinal mirror motion induced by an excitation signal sent to the mirror or marionette controls. The actuation response, in m V^{-1}, can be written as the product of two TFs: $A_i \times P_i$ where P_i is the pendulum mechanical model. For a better view of the measurements, only the part A_i is shown in the following figures. The full actuation TF, $A_i \times P_i$, permits us to convert the input signal channel into the induced mirror motion with absolute timing using the GPS as reference.

When taking science data, the suspension electronics is set in the LN mode. The mirror actuation TF that is needed is thus the one using the LN mode electronics. However, the range of the mirror actuation in the LN mode is too low for direct measurements. The measurements are thus done in different steps described in the following paragraphs:

- the actuation TF is measured in the HP mode from free swinging Michelson data,
- the LN/HP actuation TF ratio is computed from measurements of the current flowing in the coils,
- the actuation TF in the LN mode is then computed combining these two measurements.

4.1. Mirror actuation TF in the HP mode

4.1.1. Procedure. Data are taken in simple Michelson configurations using a single mirror in each arm: the other arm mirror and the PR mirror are misaligned as shown in figure 3. The ITF is working in an open loop: no correction is applied to the mirrors nor marionettes. Some sinusoidal signals (so-called *lines* it the following) zN are applied to the mirror actuators set in the HP mode.

The mirror motion ΔL_{rec} is reconstructed using the technique described in section 3, taking into account the ITF optical response and the output power sensing. Only good-quality data with a coherence higher than 70% between the excitation zN and ΔL_{rec} are selected to compute a first TF: $H = \Delta L_{\mathrm{rec}}/zN$ in m V^{-1}. Simulations were used to determine the errors of the TF modulus M and phase P (rad) from the coherence C of the measurements as

$$\frac{\Delta M}{M} = a\sqrt{\frac{1-C}{C}}\frac{1}{\sqrt{n_{\mathrm{av}}}} \tag{6}$$

$$\Delta P = b\sqrt{\frac{1-C}{C}}\frac{1}{\sqrt{n_{\mathrm{av}}}} \tag{7}$$

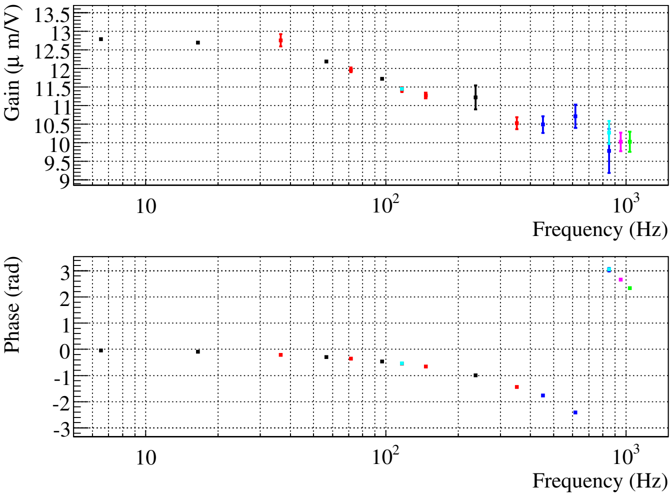

Figure 7. Typical mirror actuation TF: WE mirror using the up–down coils in the HP mode, 1 September 2009 (the pendulum response is not included).

where n_{av} is the number of averages performed on the TF and a and b two constants respectively estimated to be 0.85 and 0.88.

4.1.2. VSR2 measurements. During VSR2, free swinging Michelson data have been taken every 2 weeks to monitor the actuation TF, and a series of pre-run and post-run measurements were done in June 2009 and January 2010. Lines were injected between 5 Hz and 2 kHz to measure the actuation response. An example of mirror actuation TF measured during VSR2 is shown in figure 7.

The linearity of the response was checked applying different amplitudes of the actuation excitation signal. The evolution of the modulus of the actuation TF as a function of the injected amplitude is shown in figure 8, along with the $\chi^2/ndof$ assuming a linear response. It indicates that the response is linear within statistical errors.

The time stability of the actuation response during VSR2 has been monitored as shown in figure 9. In most cases, the $\chi^2/ndof$ assuming a constant response indicate that the modulus and phase are compatible with a constant during VSR2. In few cases, time variations of the modulus were observed, but still below 1%. The actuation TF modulus and phase have thus been time-averaged. Below 900 Hz, the statistical errors at the frequencies monitored during VSR2 are below 1% in the modulus and 10 mrad in phase. Between 900 Hz and 2 kHz, they are estimated to be 3% and 30 mrad.

4.2. LN/HP mirror actuation TF ratio

4.2.1. Procedure. The ratio of the LN to HP mirror actuator TF is necessary to convert the mirror actuation from the HP TF to the LN TF. The differences of the actuation in both modes come from the different gains and filters in the DSP, different DACs and different paths in the coil driver analog electronics. The coupling of the coil-induced magnetic field with the mirror magnets and the pendulum response are not modified. A direct way to measure the ratio is thus to inject an excitation zN at the actuation input (with no control signal), and measure the current C flowing in the coils in HP and in LN modes.

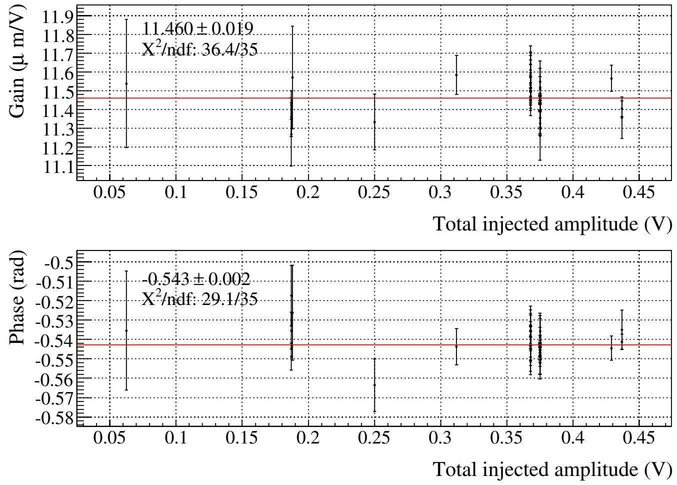

Figure 8. Linearity of the mirror actuation TF (WE mirror using the up–down coils in the HP mode) measured from June 2009 to January 2010: TF versus excitation amplitude (at 117 Hz). The average modulus and phase values are given and shown as the red line.

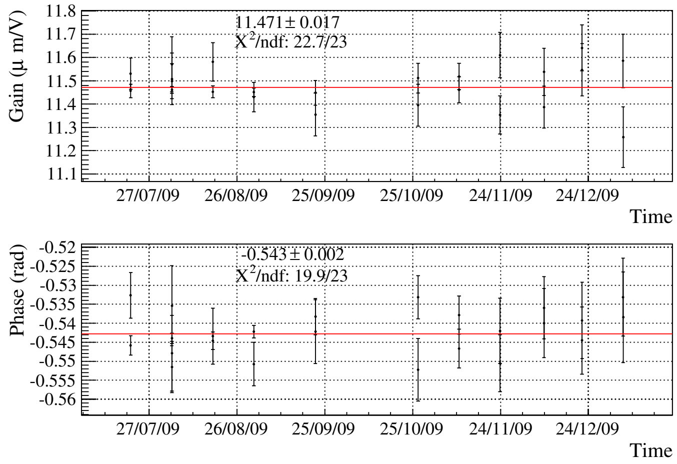

Figure 9. Stability of a mirror actuation TF (WE mirror using the up–down coils in the HP mode) during VSR2, shown at 117 Hz. The average modulus and phase values are given and shown as the red line.

The ratio of the TFs C_{LN}/zN to C_{HP}/zN is a measurement of the actuator LN/HP ratio. Since the current is measured through the same resistor and ADC whatever the mode is, its sensing response cancels out in the ratio. Such measurements were performed every week during VSR2.

4.2.2. VSR2 measurements. An example of the LN/HP ratio measured during VSR2 is shown in figure 10.

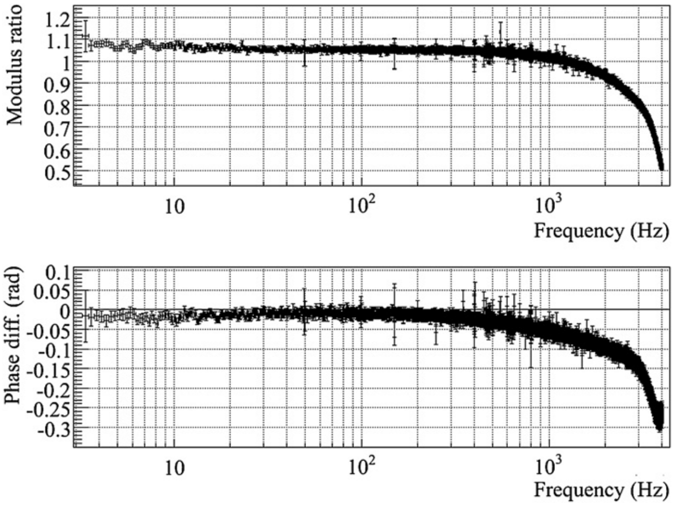

Figure 10. LN to HP ratio measurement (WE mirror, coil up, 1 September 2009).

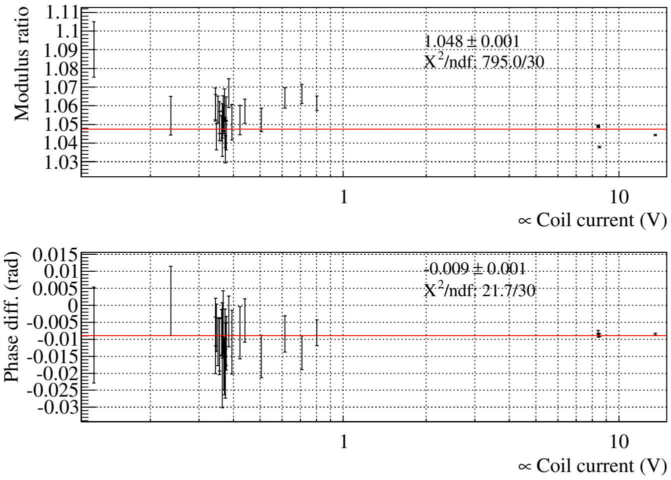

Figure 11. Linearity of the LN to HP ratio (WE mirror, coil up) measured from June 2009 to January 2010: TF ratio versus excitation amplitude (at 117 Hz). The average modulus and phase values are given and shown as the red line. The χ^2/ndf assuming linearity is given.

Different amplitudes of the excitation were tested before and after VSR2 in order to check the linearity and non-saturation of the electronics as shown in figure 11. Only 3 coil actuations out of 12 present possible nonlinearities which are nevertheless lower than 1.5% in the modulus and 10 μs in the phase[22]. These numbers are conservatively used as systematic errors for all mirror actuations.

---

[22] The phase nonlinearities are frequency dependent and have been estimated as a delay $t_d = \phi/(2\pi f)$.

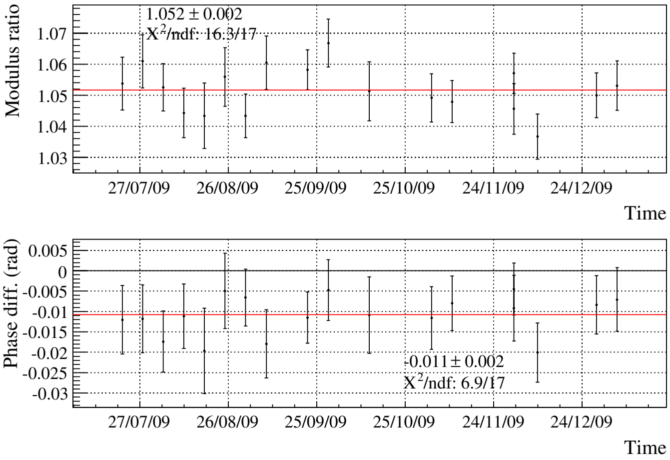

Figure 12. Stability of the LN to HP ratio (WE mirror, coil up) during VSR2, shown at 117 Hz. The average modulus and phase values are given and shown as the red line. The χ^2/ndf assuming a constant response is given.

The stability of the LN/HP ratio was monitored during VSR2 as shown in figure 12. Since no time variation was found, the measurements have been time-averaged. The statistical errors are below 1% in the modulus and 10 mrad in the phase up to a few kHz.

4.3. Mirror actuation TF in the LN mode

The mirror actuation TF in the LN mode can be derived multiplying the averaged actuation TF in the HP mode and the averaged LN/HP TF ratio. Only the statistical errors are used. The modulus and phase of the obtained TF are then fit simultaneously with a parameterization including the nominal DAC anti-imaging filter (sixth order elliptical filter with a cut-off at 3.7 kHz) as well as free parameters: a gain, a delay and simple poles and simple zeros. Poles and zeros are arbitrarily added such that the fit matches the data with a high χ^2 probability: the residuals are thus within the statistical errors of the order of 1.4%/14 mrad in the modulus and phase below 900 kHz and of 3.2%/32 mrad up to 2 kHz.

The example of the WE mirror actuation TF data, fit and residuals in the LN mode is shown in figure 13. The fit results in a dc gain of $13.33 \pm 0.02\,\mu\mathrm{m\ V}^{-1}$, in agreement with the expected value. The fit χ^2 is 48.0 for 88 degrees of freedom. It indicates that the parameterization is compatible with the data. Similar results have been obtained on the other mirror actuations [14]. Therefore no additional systematic error on the actuation in the LN mode is estimated from the fit residuals.

The measured actuation TFs are all superposed in figure 14. The shape of the TF modulus was expected to be flat from the electronics point of view. However, a frequency dependence has been observed, which is different for the BS actuation compared to the other mirror actuation. It is explained by the presence of eddy currents induced in the reference mass (RM) by the coil current. The shape and order of magnitude of the effect is in agreement with finite element simulations of the system. The effect is expected to be lower for the BS mirror since the RM is made of aluminum while the arm RMs are made of stainless steel. The geometry of the coil supports also induces lower eddy currents in the BS RM. The data confirm this qualitative expectation.

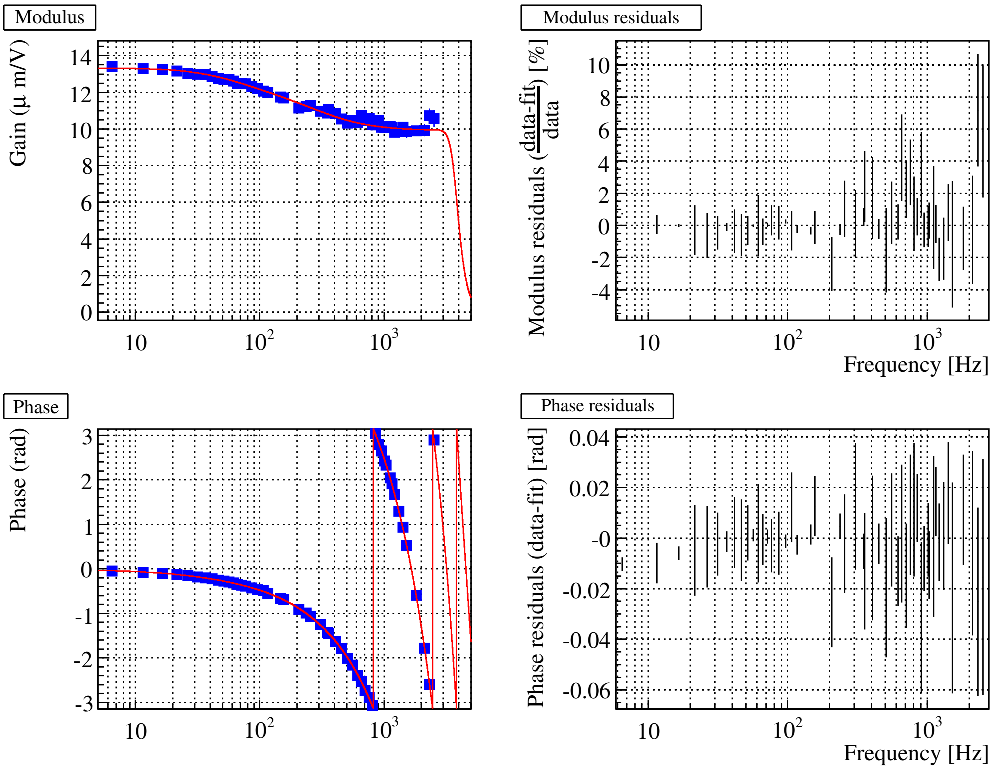

Figure 13. WE mirror actuation in the LN mode. On the left column, the modulus and phase measurements are given (blue squares) along with the fitted parameterization (red curve). On the right column, the modulus and phase residuals of the parameterization are shown. The fit results in a dc gain of $13.33 \pm 0.02\,\mu\mathrm{m\ V}^{-1}$, two simple poles and two simple zeros around 70 Hz and 80 Hz, and 300 Hz and 350 Hz, respectively, and a delay of $271.3 \pm 0.7\,\mu$s.

In the 1–2 kHz region, the modulus of the mirror actuation responses tends to increase by a few percents. This might be related to the excitation of internal modes of the mirrors [15]. For the end mirrors, the resonance frequencies are close to 5.5 kHz for the drumhead mode and to 3.9 kHz for the butterfly mode.

4.3.1. Estimation of systematic errors.

Free swinging Michelson in the LN mode. Direct measurements of the mirror actuation TF in the LN mode have been performed below 100 Hz using free swinging Michelson data. Due to the low mirror excitation level in the LN mode, it was only possible to get measurements for the BS mirror. The comparison with the LN actuation TF of the BS mirror obtained by the main method is shown in figure 15. It did not indicate any systematic difference within the statistical errors of the order of 5% on the modulus and 50 mrad on the phase.

Estimated errors. The statistical and systematic errors obtained on the BS and end mirrors actuation TF measurements during VSR2 are summarized in table 1.

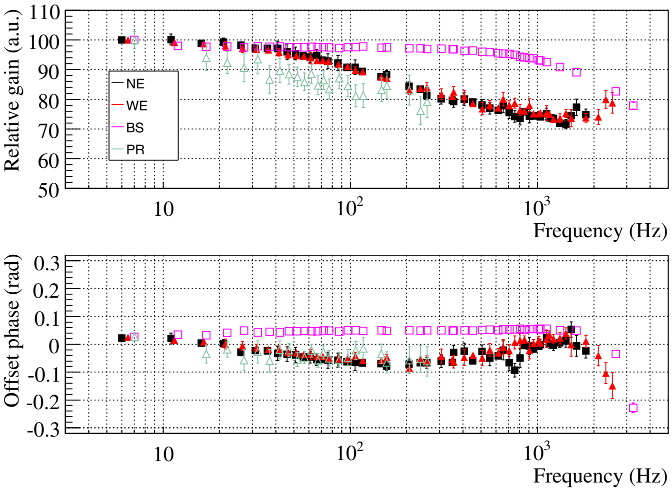

Figure 14. Measured mirror actuation in the LN mode. The modulus have been normalized to the fitted dc gain. For better visibility, a delay of (270 + 180) μs has been subtracted from the phase (∼180 μs is introduced by the DAC anti-imaging below 1 kHz. 270 μs is close to the delays fitted on the measurements). The statistical errors are shown. WE: black squares, NE: red full triangles, BS: pink empty squares, PR: green empty triangles.

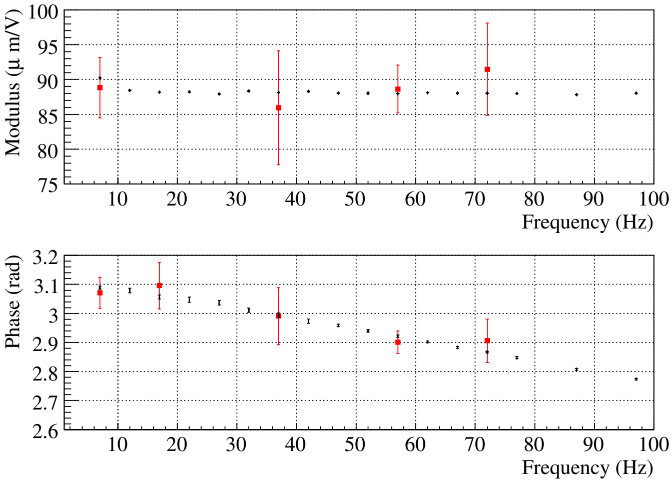

Figure 15. Comparison of the BS mirror actuation response measured with (black) the standard method and (red squares) direct measurements with free swinging Michelson data.

Table 1. Statistical and systematic errors of mirror actuation TF measurements.

	5 Hz to 900 Hz		900 Hz to 2 kHz	
	Statistical	Systematic	Statistical	Systematic
Modulus	1.4%	2.5%	3.1%	2.5%
Phase	14 mrad	10 μs	31 mrad	10 μs

The statistical error is quadratically summed to the systematic error to estimate the error on the mirror actuation modulus to 3% below 900 Hz and 4% above. The phase error is dominated by a constant phase of 14 mrad below ~200 Hz and by a delay of 10 μs above.

4.4. PR mirror actuation TF

Since the PR mirror cannot be calibrated from a free swinging Michelson configuration, an indirect method has been used.

First, the ratio of the PR actuation TF to the BS actuation TF is extracted locking the PR–WI cavity: the BS is used as a folding mirror. A motion of PR, BS or WI has the effect of changing the length of the cavity. This can be sensed by the photodiode at the ITF output, which is used for the locking of the cavity. Adding the same signal to the corrections sent to BS or PR has the same effect in terms of changing the cavity length (i.e. the optical response), provided a factor $\sqrt{2}$ is taken into account because of the 45° orientation of the BS mirror.

Two datasets were taken at the end of VSR2. One with excitation injected on the PR mirror actuation and one with excitation injected on the BS mirror actuation. The TFs of the excitation zN to the ITF output $\mathcal{P}_{\mathrm{ac}}$ can be written as

$$\mathrm{TF}\left[\frac{\mathcal{P}_{\mathrm{ac}}}{zN_{PR}}\right] = \frac{SOP_{\mathrm{PR}}A_{\mathrm{PR}}}{1-G_{\mathrm{olg}}}$$

$$\mathrm{TF}\left[\frac{\mathcal{P}_{\mathrm{ac}}}{zN_{\mathrm{BS}}}\right] = \frac{SOP_{\mathrm{BS}}A_{\mathrm{BS}}}{1-G_{\mathrm{olg}}}$$

with the open-loop gain $G_{\mathrm{olg}} = SO\sum_i P_iA_iF_i$ where i stands for the three mirrors of the cavity. The sensing response S and the optical response O are the same for all the mirrors as well as the pendulum mechanical response P_i. The ratio of both TFs thus gives a measurement of A_{PR}/A_{BS}. The ratio has been measured below 300 Hz with statistical errors of the order of 5%/50 mrad.

As as second step, the ratio is multiplied by the BS actuation TF to get the PR actuation TF. The shape of the PR mirror actuation is shown in figure 14. Below 300 Hz it is compatible with the arm mirror actuation TFs, as expected since they have the same design.

4.5. Marionette actuation TF

4.5.1. Procedure. Due to the low-pass mechanical response of the double-stage pendulum, the marionette actuation TF cannot be measured directly using free swinging Michelson data. The actuation TF is thus measured in two steps. Once the mirror actuation TF is computed, the ratio of the marionette actuation TF to the mirror actuation TF is measured. The marionette actuation is then derived.

Excitation has been injected on a mirror and then on its marionette while the ITF is locked as in the *science mode*. Using the description from figure 2, the actuation channels are respectively called k_{mir} and k_{mar} in the following. The TFs $T_{k_{\mathrm{mir}}}$ and $T_{k_{\mathrm{mar}}}$ from the excitation zN to the ITF output can be written as

$$T_{k_{\mathrm{mir}}} = \mathrm{TF}\left[\frac{\mathcal{P}_{\mathrm{ac}}}{zN_{k_{\mathrm{mir}}}}\right] = \frac{SO_kP_{k_{\mathrm{mir}}}A_{k_{\mathrm{mir}}}}{1-G_{\mathrm{olg}}}$$

$$T_{k_{\mathrm{mar}}} = \mathrm{TF}\left[\frac{\mathcal{P}_{\mathrm{ac}}}{zN_{k_{\mathrm{mar}}}}\right] = \frac{SO_kP_{k_{\mathrm{mar}}}A_{k_{\mathrm{mar}}}}{1-G_{\mathrm{olg}}}$$

with the open-loop gain $G_{\mathrm{olg}} = S\sum_i O_iP_iA_iF_i$. Since the excitation is injected on the mirror and its marionette, the ITF optical response is the same for both. The actuation TF ratio,

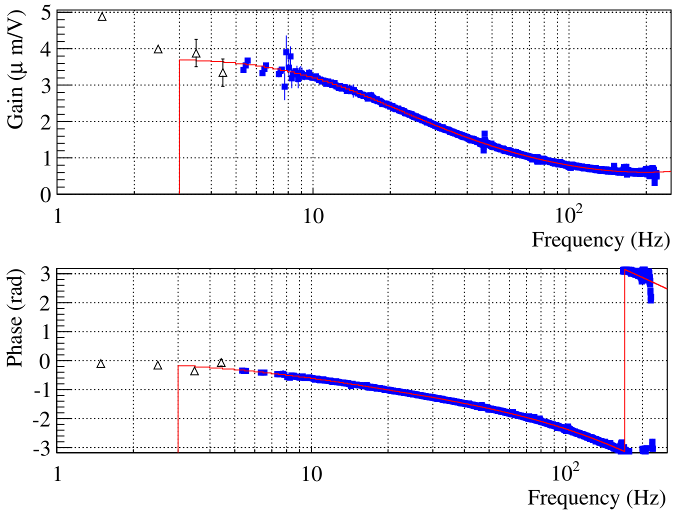

Figure 16. WE marionette actuation TF. Blue squares: measured modulus and phase. Red curve: the fitted model (shown for $f > 3$ Hz). Empty triangles: direct measurements using free swinging Michelson data are also shown for comparison.

corrected for the different responses of the pendulum to the mirror and marionette motions, is then derived as

$$\frac{A_{k_{\rm mar}}}{A_{k_{\rm mir}}} = \frac{P_{k_{\rm mir}}}{P_{k_{\rm mar}}} \frac{T_{k_{\rm mar}}}{T_{k_{\rm mir}}}.$$

The marionette actuation TF $A_{k_{\rm mar}}$, in m $\rm V^{-1}$, is then computed multiplying this ratio by the parameterization of the corresponding mirror actuation TF $A_{k_{\rm mir}}$.

4.5.2. VSR2 measurements. The controls of the end mirrors through the marionettes are negligible above a few 10s of Hz. During VSR2, they have thus been measured from 5 to 200 Hz.

Different amplitudes of the excitation signal were tested. No nonlinearities in the ratio of the marionette to mirror actuation responses were observed within statistical errors. Since no time variations were observed in the weekly monitoring during VSR2, the measurements have been averaged. The statistical errors of the ratio are of the order of 3% in the modulus and 30 mrad in the phase.

The example of the WE marionette actuation TF and fit is given in figure 16. The TF has been fit from 5 to 150 Hz, with free parameters: a gain, a delay and simple and complex poles and zeros. The fit residuals are within statistical errors up to 100 Hz. Similar results were obtained on the NE marionette [14].

4.5.3. Marionette actuation systematic errors. Since the parameterization of the mirror actuation TF is used to measure the marionette actuation TF, the systematic errors are at least the errors from this parameterization: 3% and 14 mrad on the modulus and the phase. Additional source of errors were searched comparing the results with other measurements.

Free swinging Michelson measurements. Direct measurements of the marionette actuation TF have been performed injecting lines to the marionette in free swinging Michelson configurations. Due to the low-pass mechanical response of the double-stage pendulum, the measurements were possible from 1.5 to 5 Hz only. The measurements are compared to the standard ones in figure 16. Since there is no frequency overlap, only a rough check that the modulus and phase do not show any offset between both measurements could be done, within errors of the order of 10% and 100 mrad respectively.

5. Output port calibration

The main ITF signal, $\mathcal{P}_{\mathrm{ac}}$, is a measurement of the power at the ITF output port (*dark fringe* signal). In this section, the stability of the Virgo timing system, which is critical for the global GW search, is first studied. The calibration of the output power sensing and its absolute timing is then described.

5.1. Virgo timing system

The Virgo data acquisition system [16] (DAQ) and timing system installed before VSR2 have been described in [17]. The timing system is based on a master timing system controlled by GPS. Its roles are to give the rhythm of the control loops and to give the time stamps to the DAQ.

The GPS receiver delivers a 1 pulse-per-second (PPS) clock and the corresponding date encoded in the IRIG-B format [18]. This signal is distributed to all active elements (i.e. ADC, DAC) located in the four ITF buildings with the same propagation delay, measured [17] to be 16.041 μs.

5.1.1. Stability of the timing system. In order to monitor the stability of the timing system over periods longer than 1 s, the 1 PPS signal delivered by an independent atomic clock is used. The delay between the start of the 1 PPS signal and the start of the new second in the Virgo data is measured [19].

The monitoring atomic clock being independent, its clock slowly drifts from the GPS reference. The drift is estimated assuming it is linear over periods of 1 day. The distribution of the delays around the average drift monitored during the full VSR2 is shown in figure 17. No tails are observed outside ± 0.3 μs, which is consistent with the precision of the IRIG-B signal of 100 ns.

As an other monitoring of the timing system, the corrections received every second by the ADC boards to resynchronize their local clock to the main 1 PPS clock have been checked [19]. No timing instabilities have been found during VSR2, within again a precision of 0.3 μs.

Over periods shorter that 1 s, the timing jitter of the main 1 PPS clock has also been measured [20] to be below $0.1\,\mathrm{ns\,Hz^{-1/2}}$, orders of magnitude below the calibration timing uncertainties.

5.2. Sensing electronics

The sensing scheme of the ITF output power is shown in figure 18. Its TF must be taken into account in the GW strain reconstruction in order not to distort the reconstructed amplitude and phase. The readout is composed of

- the photodiodes and the analog electronics;

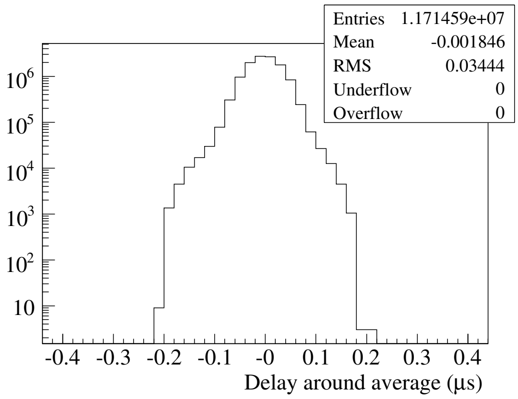

Figure 17. Fluctuations of the delays measured between the Virgo timing system and the drift-corrected atomic clock. Data during *science mode* segments of VSR2 have been used.

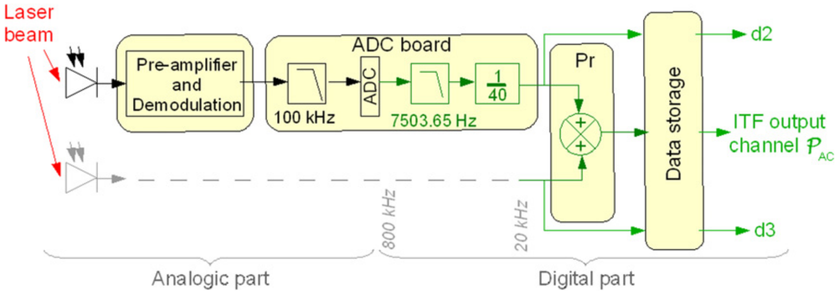

Figure 18. Overview diagram of the sensing of the ITF output power sampled at 20 kHz.

- the ADC board with (i) an analog anti-alias filter (sixth order Butterworth filter) with a cut-off frequency at 100 kHz, (ii) the ADC sampling the signal at 800 kHz, (iii) a digital eighth order Butterworth filter with the cut-off frequency at 7503.65 Hz, (iv) a digital decimation of the signal at 20 kHz picking 1 sample over 40 (the last sample of the 40 of the window is kept) and (v) time stamping;
- the DAQ to store the data. It does not introduce any delay.

The response of the photodiode and analog electronics before the ADC board is assumed to be flat in the frequency band of Virgo and to introduce negligible delays. The response of the ADC board analog anti-alias filter was measured to be equivalent to a delay of 5.7 ± 0.2 μs below 10 kHz. The response of the digital processes has been precisely checked and can be perfectly modeled up to 10 kHz by the digital Butterworth filter and an advance of 48.75 μs, introduced by the digital decimation. Below 2 kHz, the Butterworth filter can be approximated by a delay of 109 ± 1 μs.

5.2.1. Timing of the readout electronics. The knowledge of the absolute delay introduced by the sensing of the output port laser power is essential in order to provide absolute timing of the Virgo data.

From our understanding of the sensing described above, the sensing below 2 kHz can be modeled by a delay of $5.7 + 109 - 48.75 = 66.0$ μs. In order to take the GPS time as reference, an advance of 16 μs must be added due to the timing distribution system: it results in a total delay of 50.0 μs.

In order to measure this delay, the 1 PPS clock from the main GPS receiver of the Virgo timing system has been reshaped to a ramp and digitized by the ADC board also used to sample the output power $\mathcal{P}_{\rm ac}$. The beginning of the ramp, estimated from a fit, indicates the time of the 1 PPS. The delay between the start of the second in the Virgo data and the 1 PPS is a measurement of the readout delay. The delay introduced by the analog part of the ADC board has been measured using the raw 800 kHz ADC values [20]. The measurement is in agreement with the expected value, within the ±4 μs systematic errors introduced by the measurement method. It has been checked that the digital processing of the 800 kHz values behaves as expected and do not introduce further timing uncertainties.

During VSR2, the 1 PPS ramped signal has been continuously sampled at 20 kHz [19]. The distribution of the measured delays around its average value has a RMS of less than 40 ns and tails within 0.3 μs, again compatible with the precision of the IRIG-B signal.

The photodiode power readout is thus known within ±4 μs and was stable within 300 ns during VSR2.

5.2.2. Models for ITF sensing. Following the studies described in the previous sections, the ITF photodiode sensing below 2 kHz can be parameterized by a simple delay of 49.3 μs, taking as reference the GPS time. The full model, valid up to 10 kHz, is a delay of -59.7 μs and an eighth order Butterworth filter with cut-off frequency at 7503.65 Hz. Systematic errors on the absolute timing are estimated to 4 μs.

6. Estimation of the sensitivity during VSR2

One of the final results of the calibration is the estimation of the detector noise level as a function of frequency, the so-called sensitivity curve. It corresponds to the noise level of the detector in terms of the GW strain signal in the frequency domain, $\tilde{h}(f)$. The sensitivity is estimated directly in the frequency domain, without reconstructing the $h(t)$ signal in the time domain. In this section, the measurement of the global response of the ITF to a GW strain is first presented and then used to estimate the sensitivity curve. The behavior of the Virgo sensitivity during VSR2 is finally described.

6.1. Virgo transfer function

The global TF of the ITF describes the path from the differential arm elongation ΔL in meter to the output power channel $\mathcal{P}_{\rm ac}$. It is measured from specific data taken with the detector in the same configuration as in the *science mode*. Excitation (colored noise) is injected to the actuation of one end mirror (for example the mirror j), through the channel zN_j (see figure 2). The inverse of the ITF TF is defined, in W m^{-1}, as

$$\mathrm{TF}\left[\frac{\mathcal{P}_{\rm ac}}{\Delta_L}\right] = \mathrm{TF}\left[\frac{\mathcal{P}_{\rm ac}}{zN_j}\right]\frac{1}{A_j P_j}.$$

The TF $\frac{\mathcal{P}_{\rm ac}}{zN_j}$ is measured directly from the data, from a few Hz to ~1.5 kHz. The mirror actuation response A_j (in the LN mode) and the pendulum mechanical response P_j are known from the actuator calibration (see section 4.3).

Above 1.5 kHz, the TF has to be extrapolated. It can be described in more detail as

$$\mathrm{TF}\left[\frac{\mathcal{P}_{\rm ac}}{\Delta_L}\right] = \frac{SO_j P_j A_j}{1 - G_{\rm olg}} \times \frac{1}{A_j P_j}.$$

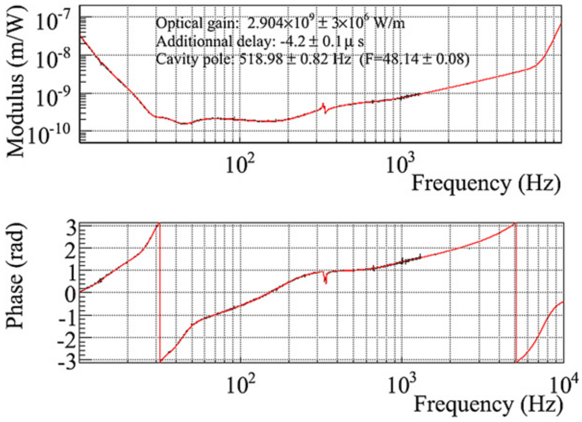

Figure 19. Virgo TF: modulus and phase in the range 10 Hz to 10 kHz (29 December 2009). The data are in black (only the points with coherence higher than 70% are shown). The continuous red line is the Virgo TF model: it is a copy of the measurements below 900 Hz, and is then extrapolated at higher frequency.

In this frequency band, the longitudinal motion of the ITF mirrors is free ($G_{\mathrm{olg}} \sim 0$): at 1 kHz, the contribution from the controls to the ITF differential motion has been estimated to be of the order of 1%. The ITF TF can thus be simply described by $S \times O_j$, the combination of the photodiode readout response and of the ITF optical response to the mirror motion. The response of the photodiode sensing has been precisely calibrated (see section 5.2).

The optical response of the ITF to a mirror displacement [21] is approximated by a simple pole whose frequency depends on the average cavity finesse following

$$f_p = \frac{c}{4LF}$$

where c is the light speed and L the cavity length (3 km). For a finesse of 50, the cavity pole is close to 500 Hz but is expected to vary by $\sim\pm 3\%$ due to the etalon effect in the input mirror varying with the mirror temperature (the input mirrors are flat–flat mirrors with non-zero reflectivity on the face with anti-reflecting coating).

In order to extrapolate the ITF TF, the measured TF is fitted from 900 Hz to ~1.5 kHz with points where the coherence is higher than 90%. The fit model is $O_j \times S$ with three free parameters: the optical gain, the pole frequency and an extra delay. The fit is then extrapolated up to 10 kHz.

6.1.1. TF during VSR2. The Virgo TF was measured once per week during VSR2, exciting the WE mirror. A typical case of the full TF model is shown in red in figure 19. The finesse is fitted between 48 and 51 for all measurements. The distribution of the fitted delays has an average of $-3\,\mu$s and a RMS of $0.5\,\mu$s. This systematic non-zero delay highlights a possible few μs error in the (WE) mirror actuation TF and/or the model used in the fit. It is well within the systematic errors estimated on both models.

The systematic errors on the ITF TF modulus below 900 Hz are dominated by the uncertainties on the mirror actuation parameterization, estimated to 3% in modulus. At higher frequencies, the parameterization uncertainties are 4% in the modulus and one has to add the errors coming from the finesse estimation uncertainties: assuming 3% error on the finesse,

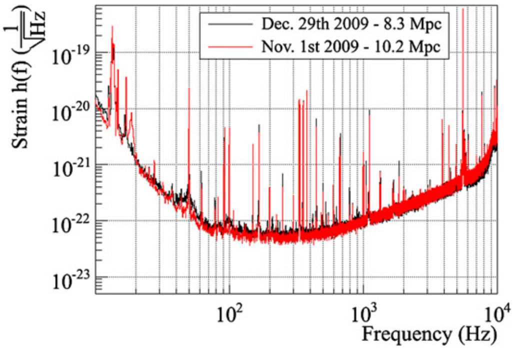

Figure 20. A typical and one of the best Virgo sensitivity curves measured in the range 10 Hz to 10 kHz, given with their associated detection range. The 50 Hz line and its harmonics are visible. The sets of permanent calibration lines used for the $h(t)$-reconstruction can be seen around 15, 95 and 355 Hz. Some other lines are used to control the Virgo lock (i.e. 379 Hz). The other lines are due to environmental noise.

it induces 0.5% uncertainty on the TF modulus. The total error on the TF modulus above 900 Hz is thus below 4.5%.

6.2. *Virgo sensitivity*

The sensitivity curve is the noise level of the GW strain signal h as the function of frequency. It is computed from the noise spectral density of the photodiode readout signal $\mathcal{P}_{\mathrm{ac}}$, in W Hz$^{-1/2}$, and the modulus of the ITF TF, in m W^{-1}, as

$$S_h(f) = \mathcal{P}_{\mathrm{ac}}(f) \times \left(TF\left[\frac{\mathcal{P}_{\mathrm{ac}}}{\Delta_L}\right]\right)^{-1}\frac{1}{L}$$

where L is the arm cavity length of 3000 m for Virgo.

6.2.1. Sensitivity during VSR2. Virgo sensitivity curves measured during VSR2 are shown in figure 20. The uncertainties on the sensitivity are directly related to the errors on the Virgo TF modulus, of the order of 3% below 900 Hz and up to 4.5% above.

The *detection range D* can be extracted as a figure of merit from the ITF sensitivity curve. It is defined [22] as the distance to which a coalescence of two compact objects of masses m_1 and m_2 is visible with a signal-to-noise ratio of 8, averaged on the source orientation and direction in the sky:

$$\frac{D}{1\ \mathrm{Mpc}} = \frac{0.5}{2.26}\int_{f_{\mathrm{min}}}^{f_{\mathrm{max}}}\frac{|\tilde{h}(f)|^2}{S_h(f)}\,\mathrm{d}f$$

where $S_h(f)$ is the properly calibrated noise one-sided power spectral density and $\tilde{h}(f)$ is the Newtonian approximation of the signal spectral density for a source at a distance of 1 Mpc:

$$|\tilde{h}(f)|^2 = \frac{5}{4}\,\frac{\pi}{6}\,\frac{G_N^{5/3}}{c^3}\,\frac{\mu M^{2/3}}{d^2}\,(\pi f)^{-7/3}$$

with $\mu = \frac{m_1 m_2}{m_1+m_2}$, $M = m_1 + m_2$, $d = 1$ Mpc, c the speed of light and G_N the gravitational constant. The value of f_{max} is set to the frequency at the innermost stable circular orbit, f_{ISCO},

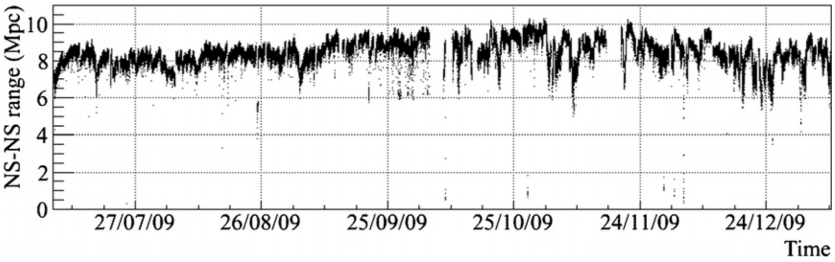

Figure 21. Virgo BNS detection range during VSR2 *science mode* data, estimated every minute.

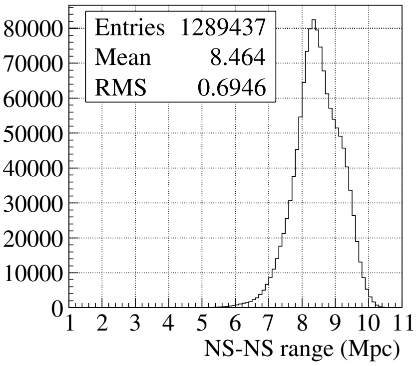

Figure 22. Distribution of Virgo BNS detection range estimated every 10 s during VSR2 *science mode* data.

defined as

$$f_{\mathrm{ISCO}} = \frac{c^3}{6\sqrt{6}\pi G_N M}.$$

In the following, $f_{\min}$ is set to 10 Hz.

The binary neutron star (BNS) detection range (for a 1.4 $M_\odot$ × 1.4 $M_\odot$ system) is used in figure 21 to show the Virgo sensitivity over time during VSR2 (149.3 days of *science mode* data). Its distribution is shown in figure 22: its average is 8.5 Mpc and its RMS 0.7 Mpc. The BNS detection ranges were between 7.1 Mpc and 9.9 Mpc for 95% of the *science mode* time. A typical and one of the best sensitivity curves are shown in figure 20. The BNS detection range is mainly sensitive to the noise level between ∼50 and ∼500 Hz, where the systematic errors, coming from $S_h(f)$, are estimated to be 4%.

The detection range computed as a function of the total mass of the binary system is shown in figure 23 for a typical sensitivity of VSR2. When the component mass is higher, the upper cut-off frequency becomes smaller: it means that the inspiral range focuses on a narrower low-frequency band of the sensitivity.

7. Summary

Calibration procedures have been developed and implemented for the Virgo ITF during its first [23] and second science runs. They are used to estimate the absolute scale of the displacements to which the ITF is sensitive, down to $\sim 10^{-19}$ m.

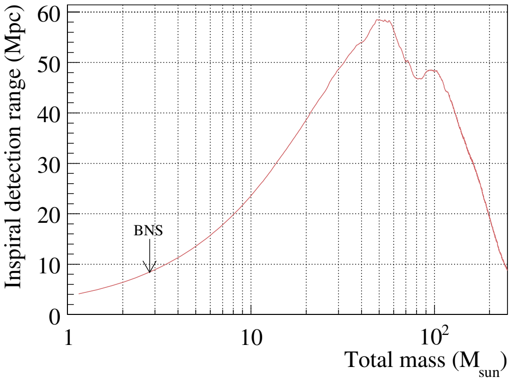

Figure 23. Virgo detection range as a function of the binary system mass M (with $m_1 = m_2 = M/2$) in the case of a typical VSR2 sensitivity (BNS detection range of 8.3 Mpc).

The methods used to measure the mirror actuation response, the ITF output power sensing and absolute timing have been shown along with their performances. The stability of the parameters during VSR2 has been checked. When available, independent measurements of the parameters are in good agreement. They are used to estimate the systematic errors which are dominant compared to the statistical uncertainties. Typical results obtained during VSR2 have been shown. An important parameterization is the mirror actuation response below 900 Hz, known within 3% in the modulus and 14 mrad/10 μs in the phase. The *dark fringe* power sensing has been measured with a timing precision of 4 μs.

The frequency-domain sensitivity estimation, $S_h(f)$, has been described. Systematic errors have been estimated to be of the order of 3% below 900 Hz, increasing up to 4.5% at higher frequencies. Typical and best sensitivities of Virgo during VSR2 have been shown. As a figure of merit, the BNS detection range of Virgo during VSR2 (149 days of *science mode* data) had an average value of 8.3 Mpc, with a RMS of 0.7 Mpc.

References

[1] Accadia T *et al* (VIRGO Collaboration) Virgo detector, *JINST* submitted
Accadia T *et al* (VIRGO Collaboration) 2010 Status and perspectives of the Virgo gravitational wave detector *J. Phys.: Conf. Ser.* **203** 012074

[2] Abbott B *et al* (LIGO Collaboration) 2009 LIGO: The Laser Interferometer Gravitational-Wave Observatory *Rep. Prog. Phys.* **72** 076901

[3] Acernese F *et al* (VIRGO Collaboration) 2010 Measurement of super-attenuator seismic isolation by Virgo interferometer *Astropart. Phys.* **33** 182–9

[4] Bernardini A *et al* 1999 Suspension last stage for the mirrors of the Virgo interferometric gravitational wave antenna *Rev. Sci. Instrum.* **70** 3463

[5] Bozzi A *et al* (VIRGO Collaboration) 2002 Last stage control and mechanical transfer function measurement of the Virgo suspensions *Rev. Sci. Instrum.* **73** 5

[6] Puppo P and Rapagnani P 2005 The electromagnetic actuators of the mirror reaction mass *Virgo Note* VIR-0016A-09

[7] Punturo M 2004 The Virgo sensitivity *Virgo Note* VIR-NOT-PER-1390-51

[8] Majorana E *et al* 2001 The beam splitter payload *Virgo Note* VIR-NOT-ROM-1390-179

[9] Acernese F *et al* (Virgo Collaboration) 2008 Lock acquisition of the Virgo gravitational wave detector *Astropart. Phys.* **30** 29–38

[10] Saulson P R 1994 *Fundamentals of Interferometric Gravitational Wave Detectors* (Singapore: World Scientific)

[11] Rolland L *et al* 2008 Mirror motion reconstruction for free swinging Michelson data *Virgo Note* VIR-0112A-08

[12] Halíř R and Flusser J 1998 Numerically stable direct least squares fitting of ellipses *Proc. 6th Int. Conf. in Central Europe on Computer Graphics, Visualisation and Interactive Digital Media (Plzen, Czech Republic)* vol 1 ed V Skala pp 125–32 (http://wscg.zcu.cz/WSCG1998/papers98/Halir_98.ps.gz)

[13] Caron B *et al* 1999 SIESTA, a time domain, general purpose simulation program for the VIRGO experiment *Astropart. Phys.* **10** 369–86

[14] Rolland L 2010 VSR2 mirror and marionette actuation calibration *Virgo Note* VIR-0076B-10

[15] Puppo P *et al* 2004 A finite element model of the Virgo mirrors *Virgo Note* VIR-NOT-ROM-1390-262

[16] Acernese F *et al* (VIRGO Collaboration) 2008 Data acquisition system of the Virgo gravitational waves interferometric detector *IEEE Trans. Nucl. Sci.* **55** 225–32

[17] Letendre N, Masserot A and Mours B 2009 Virgo+ timing deployment *Virgo Note* VIR-073B-08

[18] http://irigb.com

[19] Rolland L *et al* 2010 Stability of the Virgo timing system during VSR2 *Virgo Note* VIR-0354A-10

[20] Rolland L 2009 Calibration status in September 2009 *Virgo Note* VIR-0576A-09

[21] Rakhmanov M *et al* 2002 Dynamic resonance of light in Fabry–Perot cavities *Phys. Lett.* A **305** 239–44

[22] Abadie J *et al* (LIGO-Virgo Collaborations) 2010 Sensitivity to gravitational waves from compact binary coalescences achieved during LIGOs fifth and Virgo's first science run arXiv:1003.2481v3 [gr-qc]

[23] Accadia T *et al* (Virgo Collaboration) 2010 Virgo calibration and reconstruction of the gravitational wave strain during VSR1 *J. Phys.: Conf. Ser.* **228** 012015